Nanoscale

PAPER

View Article Online
View Journal | View Issue

Cite this: *Nanoscale*, 2018, **10**, 13539

Design and synthesis of interconnected hierarchically porous anatase titanium dioxide nanofibers as high-rate and long-cycle-life anodes for lithium-ion batteries†

Min Su Jo,‡[a] Gi Dae Park,‡[b] Yun Chan Kang *[b] and Jung Sang Cho*[a]

Received 27th February 2018,
Accepted 26th June 2018

DOI: 10.1039/c8nr01666f

rsc.li/nanoscale

We suggest an efficient and simple synthetic strategy to prepare interconnected hierarchically porous anatase TiO_2 (IHP-A-TiO_2) nanofibers by two synergetic effects: phase separation between polymers and relative humidity control during electrospinning. The macro channels formed by polystyrene decomposition were interconnected by numerous mesopores that were formed by evaporation of infiltrated water vapor in the structure. The resulting IHP-A-TiO_2 nanofibers showed better Li^+ ion storage performances than the TiO_2 materials reported in the literature. The discharge capacity of IHP-A-TiO_2 nanofibers for the 3000th cycle at 1.0 A g^{-1} and corresponding coulombic efficiency from the 20th cycle onward were 142 mA h g^{-1} and >99.0%, respectively. Well-interconnected, ultrafine TiO_2 nanocrystals within the nanofiber showed structural stability during cycling and facilitated facile charge transfer at the electrode–electrolyte interface.

Introduction

Porous structures have attracted significant attention because of their unique properties, which are induced by their large surface to volume ratio; these properties are distinct from those of their bulk counterparts.[1–3] Therefore, porous nanomaterials with various compositions have been widely studied for applications that benefit from a high porosity, such as gas sensors, catalysts, magnetics, biomedical devices, and energy storage devices.[4–8] Accordingly, many synthesis strategies, such as catalytic activation, electrochemical anodization, polymer blend carbonization, freeze drying, template-assisted approaches, and template-free Kirkendall diffusion methods, have been examined for porous nanomaterials.[9–14]

One dimensional (1-D) electrode nanomaterials with porous structures have been thoroughly researched using electrospinning processes, particularly for applications in lithium-ion batteries (LIBs).[15–17] These porous 1-D electrodes could provide efficient electron transport along the longitudinal direction, accommodate large volume expansion during repeated cycles, and allow fast Li^+ ion diffusion upon cycling because of the increased contact area between the electrolyte and electrode.[18–26] For example, Yu *et al.* synthesized bamboo-like Sn–C composited nanofibers with a porous structure by encapsulating Sn@C nanoparticles in hollow C nanofibers. This structure showed a high reversible capacity of 737 mA h g^{-1} after 200 cycles at 0.5 C.[24] Ji *et al.* also prepared porous carbon nanofibers by carbonizing electrospun polyacrylonitrile (PAN)/SiO_2 composite nanofiber, followed by removing SiO_2 nanoparticles using HF. The porous carbon nanofibers provided a reversible capacity of 593 mA h g^{-1} at the first cycle; the capacity decreased to 380 mA h g^{-1} after the 10th cycle at a current density of 50 mA g^{-1}, which accounts for 36% of that for the first cycle.[25] Additionally, Cho *et al.* exploited the Kirkendall diffusion effect to prepare a 1-D nanostructure comprising porous Fe_2O_3/Se composite nanorods with numerous nanovoids. The nanofibers exhibited a discharge capacity of 1456 mA h g^{-1} during the 400th cycle at a high current density of 1.0 A g^{-1}.[26] However, it is relatively difficult to produce pores that are exposed to the fiber surface and interconnected in the structure; in most cases, these lead to sluggish mass transport of Li^+ ions, producing anodes with a poor rate capability in LIBs. Therefore, a new strategy must be developed to interconnect the pores and produce surface-exposed pores for applications in devices that are improved by highly porous materials, including LIBs.

[a]*Department of Engineering Chemistry, Chungbuk National University, Chungbuk 361-763, Republic of Korea. E-mail: jscho@cbnu.ac.kr; Fax: (+82) 43-262-2380*

[b]*Department of Materials Science and Engineering, Korea University, Anam-Dong, Seongbuk-Gu, Seoul 136-713, Republic of Korea. E-mail: yckang@korea.ac.kr; Fax: (+82) 2-928-3584*

†Electronic supplementary information (ESI) available. See DOI: 10.1039/c8nr01666f

‡These authors contributed equally to the work.

In this study, we suggest a new efficient and simple synthetic strategy to prepare interconnected hierarchically porous metal oxide nanofibers. Porous metal oxides have not been synthesized using the two synergetic effects of phase separation between the polymers and relative humidity (RH) control during electrospinning. The approach is eco-friendly because it requires fewer steps and inexpensive, and it does not use chemicals for etching. Anatase TiO_2 was selected as the first target material because it is the most widely studied semiconducting metal oxide based on its diverse potential for many applications, such as photocatalysis, sensors, solar cells, and anodes for Li^+ ion storage.[27–34] The stacking of the zigzag chain crystals of anatase TiO_2 could facilitate intercalation/deintercalation of Li^+ ions during cycling.[29,35] We added polystyrene (PS) as a dispersed phase in the spinning solution, which generated channels in the structure during the heat treatment. Additionally, electrospinning was conducted at a high RH of 60% to induce water vapor phase separation and form numerous mesopores to interconnect the channels formed by PS decomposition. The formation mechanism of the interconnected hierarchically porous anatase TiO_2 (IHP-A-TiO_2) nanofibers was investigated in detail, and their electrochemical properties were studied for applications as anode materials in LIBs.

Experimental section

Sample preparation

IHP-A-TiO_2 nanofibers were prepared using electrospinning and a subsequent heat treatment. First, precursor nanofibers composited with TBT ($C_{16}H_{36}O_4Ti$, Kanto Chemical Co., Inc., 97.0%), PAN (Sigma-Aldrich, M_w: 150 000), and PS (Sigma-Aldrich, M_w: ~192 000) were prepared using an electrospinning process. The spinning solution was prepared by dissolving 3.0 g of PS, 2.0 g of PAN, 2 mL of TBT, and 2 mL of acetic acid (Daejung Chemicals and Metals, 99.7%) in 40 mL of *N*,*N*-dimethylformamide (DMF, Samchun Chemical, 99.5%) with vigorous stirring overnight. The prepared solution was loaded into a plastic syringe equipped with a 23-gauge stainless-steel needle. The solution was subsequently delivered at a flow rate of 2 mL h^{-1} and electrospun onto a drum collector covered with aluminum foil. During the electrospinning process, the distance between the tip and the collector was maintained at 15 cm, while the rotation of the drum was maintained at 150 rpm. The applied voltage between the collector and the needle tip was 20 kV. To introduce pores into the nanofibers, the RH was fixed at either 15 or 60% during the electrospinning process. The as-spun TBT-PAN-PS composite nanofibers were stabilized at 100 °C for 6 h and then heat-treated to 500 °C (heating rate of 5 °C min^{-1}) under air and maintained at that temperature for 3 h.

Characterizations

The crystal structures of the TiO_2 samples were investigated by X-ray diffraction (XRD, Bruker AXS, D8 Discover with GADDS). The morphologies of the samples were observed by scanning electron microscopy (SEM, TESCAN VEGA3 SBH), field emission SEM (FE-SEM, Zeiss, ULTRA PRUS), and high-resolution transmission electron microscopy (HR-TEM, JEOL, JEM-2100F) at a working voltage of 200 kV. X-ray photoelectron spectroscopy (XPS, Thermo Scientific, K-Alpha) was performed using Al-Kα radiation (1486.6 eV). Thermogravimetric (TG) analysis (TA Instruments Q600, PH407) was performed in air at a heating rate of 10 °C min^{-1} to determine the carbon content in the TiO_2 nanofibers. The surface areas of the microspheres were determined using the Brunauer–Emmett–Teller (BET) method, where N_2 was used as the adsorbate gas.

Electrochemical measurements

The electrochemical properties of the interconnected hierarchically porous anatase TiO_2 nanofibers were analyzed by constructing a 2032-type coin cell. The anode was prepared by mixing the active material, carbon black, and sodium carboxymethyl cellulose in a weight ratio of 7 : 2 : 1, respectively. Li metal and a microporous polypropylene film were used as the counter electrode and the separator, respectively. The electrolyte was 1 M $LiPF_6$ in a 1 : 1 (vol/vol) mixture of fluoroethylene carbonate/dimethyl carbonate. The charge/discharge characteristics of the samples were determined through cycling from 1.0 to 3.0 V. Cyclic voltammograms (CVs) were measured at a scan rate of 0.1 mV s^{-1}. The negative electrode was 1.4 cm × 1.4 cm, and the mass loading of the active materials was approximately 1.4 mg cm^{-2}. Alternating-current electrochemical impedance spectroscopy (EIS, ZIVE SP1) was performed from 0.01 Hz to 100 kHz.

Results and discussion

IHP-A-TiO_2 nanofibers were prepared by phase separation between polymers in the spinning solution with RH control during the electrospinning process and subsequent heat treatment. Scheme 1 describes the detailed evolution process of interconnected hierarchical pore formation in the electrospun nanofiber. The spinning solution contained PAN, PS, and TBT dissolved in DMF and was electrospun at a high RH of 60%. PS and PAN do not form a compatible polymer blend because of their different solubility parameters (PAN: 12.5 (cal $cm^{-3})^{1/2}$, PS: 9.1 (cal $cm^{-3})^{1/2}$), which induces phase separation in the spinning solution (Scheme 1-①).[36] The major component mixed with PAN and TBT forms a continuous phase, and the subcomponent PS forms a dispersed phase as an island shape in the solution. Therefore, the dispersed PS phase is stretched along the fiber length direction in the continuous PAN/TBT composite phase under electrical force during electrospinning (Scheme 1-②). The spinning was simultaneously performed under a high RH, and mutual diffusion and penetration of DMF and water vapor of the nonsolvent of the polymers occurred at the jet skin–air interface during spinning. In this step, the DMF solvent has a low vapor pressure (0.36 kPa at 20 °C) and does not quickly solidify the jet; thus, water vapor

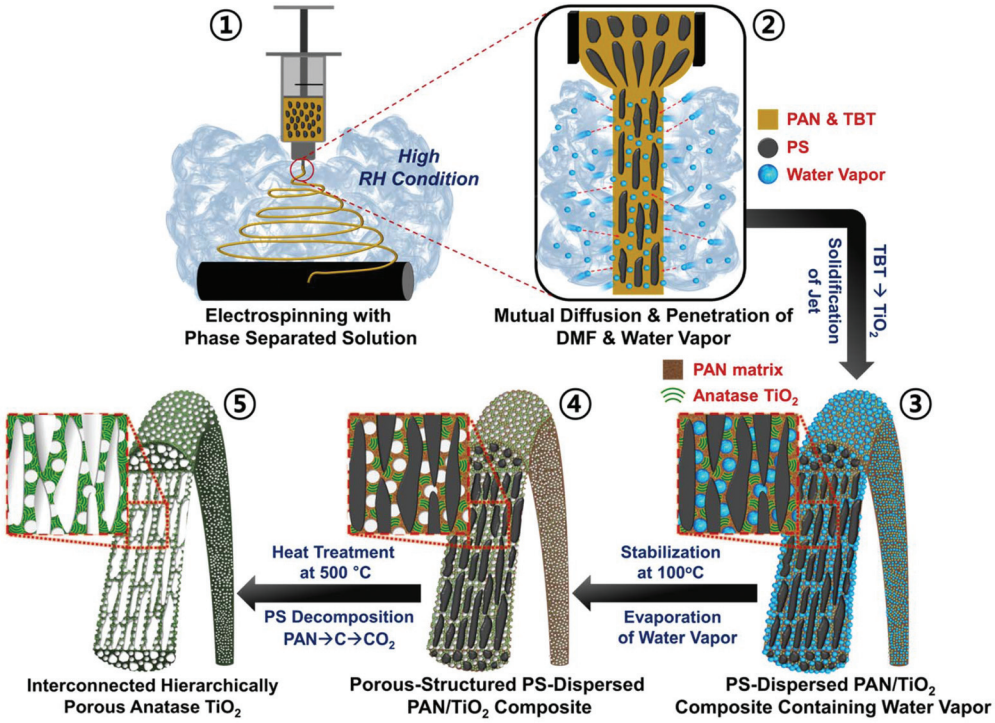

Scheme 1 Formation mechanism of IHP-A-TiO_2 nanofibers electrospun from the solution containing PAN, TBT, and PS at high relative humidity condition.

with a higher vapor pressure (2.34 kPa) could efficiently penetrate the jet.[37,38] Additionally, the discharge of the jet and the resultant charge of water vapor could provide a significant drive for successive diffusion of water vapor into the jet.[38] Thereafter, TBT in the jet was hydrolyzed to ultra-fine TiO_2 nanocrystals upon contact with water vapor because TBT is very sensitive to water and easily hydrolyzed.[39,40] Subsequently, the jet solidified to nanofibers containing water vapor because of DMF volatilization during spinning. Water vapor-induced phase separation between the polymers and vapor occurred in the as-spun PS-dispersed PAN/TiO_2 composited nanofibers (Scheme 1-③). During stabilization at 100 °C, the water vapor that infiltrated the structure evaporated and formed numerous mesopores in the composite nanofibers (Scheme 1-④). During the simple heat treatment at 500 °C, PAN first carbonized and then decomposed into CO_2 gas. Concurrently, numerous longitudinal channels were generated from decomposition of the dispersed PS phase stretched along the fiber length direction, creating porous TiO_2 nanofibers (Scheme 1a-⑤). The synergetic effects of the two kinds of phase separation caused PS decomposition, which formed macro channels; the macro channels were interconnected by numerous mesopores that were formed by evaporation of the water vapor that had infiltrated the structure. Consequently, IHP-A-TiO_2 nanofibers could be synthesized using the two synergetic phase separation effects, as described in Scheme 1.

Fig. 1 shows the morphological features of the as-stabilized nanofibers prepared from solutions with and without the PS under different RH conditions during the spinning process, and subsequently heat-treated nanofibers. The synergetic effects of polymer phase separation and RH condition during spinning on the morphology of the nanofibers were examined in detail to obtain IHP-A-TiO_2 nanofibers. Fig. 1a shows the as-stabilized PAN-TiO_2 composite nanofibers electrospun from a solution without the PS phase at a low RH of 15% during electrospinning. The nanofibers were uniform in size, with a mean diameter of 230 nm, and showed a smooth fiber surface without any noticeable pores. The sintered nanofibers also showed dense morphologies with large crystal grains, as shown in Fig. 1b. However, the nanofibers electrospun from the above solution at a high RH of 60% exhibited clear interior and exterior pores along the fiber cross section; these pores formed because of the high RH (Fig. 1c). The water that infiltrated the structure during electrospinning evaporated and generated numerous mesopores in the structure after stabilization. As a result, porous-structured TiO_2 nanofibers (P-TiO_2) were obtained after the heat treatment (Fig. 1d). In the same manner, electrospinning was carried out using the DMF solution with PAN, TBT, and the PS phase at a low RH (Fig. 1e) to examine the effect of adding the PS phase as a dispersed component in the polymer blend with PAN on the fiber morphology. The as-stabilized nanofibers had a smooth fiber surface because pores did not form by water vapor-induced phase separation. After heat-treatment, the nanofibers showed tube-like hollow structure in Fig. 1f and S1.† During electrospinning, polymer phase separation between PAN and PS

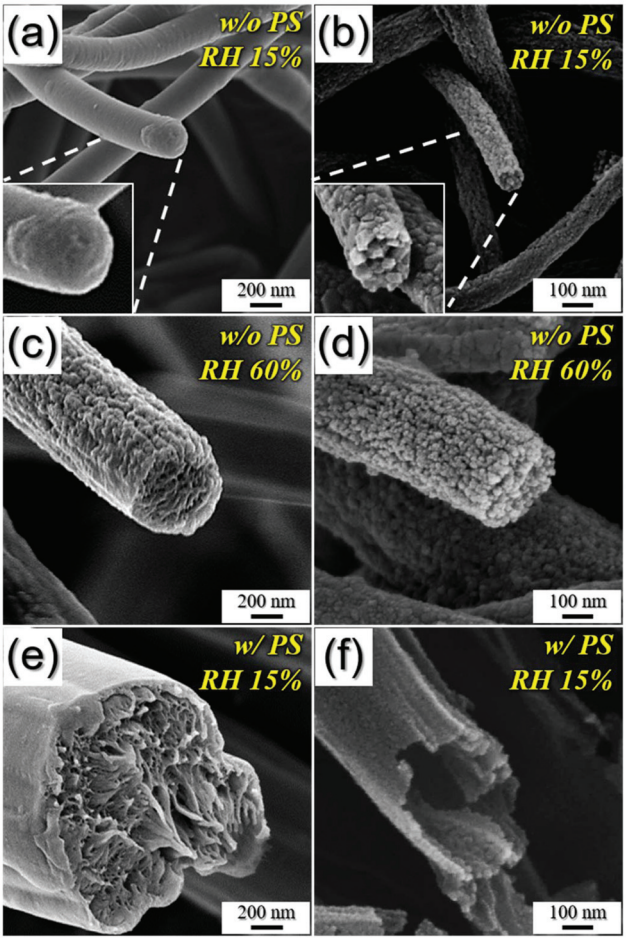

Fig. 1 Morphologies of (a, c, e) as-stabilized nanofibers and (b, d, f) sintered nanofibers electrospun from the DMF solution containing PAN, TBT and with (e, f) and without (a–d) PS phase at (c, d) high and (a, b, e, f) low RH conditions during spinning process.

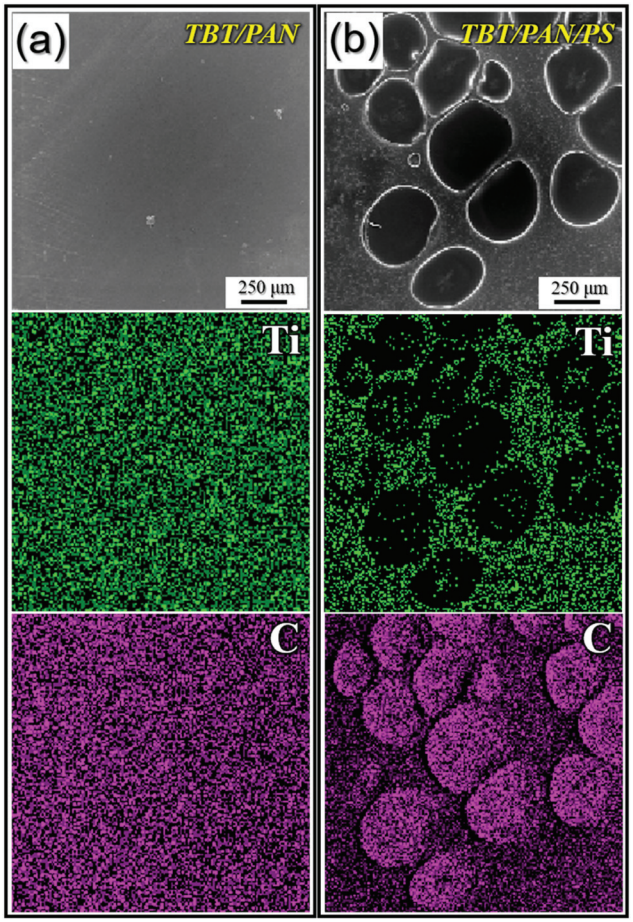

Fig. 2 SEM images and elemental mapping images of phase morphology in blends; (a) TBT/PAN, (b) TBT/PAN/PS.

occurred because of the low compatibility of this polymer blend in the spinning solution based on their different solubility parameters.[36,41] During the heat treatment, PS in the core decomposed into gaseous product, which resulted in the hollow space formation at the centre in the sintered nanofiber. At the same time, decomposition of PAN into CO_2 and sintering of TiO_2 occurred concurrently at the shell part, which formed the TiO_2 shell, as shown in Fig. 1f and S1.† PAN and TBT are well blended in the DMF solvent (Fig. 2a). However, each PS phase is dispersed as an island shape in the continuous PAN/TBT mixed phase in the blend, as shown in Fig. 2b. Therefore, the dispersed PS phase located at the core was surrounded by the PAN/TiO_2 composite in the stabilized nanofibers.

Finally, IHP-A-TiO_2 nanofibers could be electrospun from the DMF solution with PAN and TBT that contained PS in the optimum ratio at a high RH of 60%. In this study, the synergetic effects of two kind of phase separations produced macro channels (formed by PS decomposition) that were interconnected by numerous mesopores (formed by evaporation of trapped water vapor in the structure). This was demonstrated by the morphological features shown in Fig. 3 and 4. Fig. 3a shows the stabilized PAN-TiO_2-PS-composited nanofibers electrospun at a high RH. As shown in Scheme 1, water vapor could effectively penetrate the jet at the jet skin–air interface during spinning. Therefore, evaporation of trapped water vapor after DMF volatilization (for solidification) generated numerous mesopores in the structure, which were clearly observed inside and outside the nanofibers after stabilization (Fig. 3a and b). The corresponding XRD pattern in Fig. 3c shows broad peaks for PAN, PS, and TiO_2.[42–44] TiO_2 materials could be formed easily by hydrolysis reaction of TBT in the humid environment. However, the broad XRD peak revealed the formation of amorphous-like TiO_2. The TG curve of the PAN-TiO_2-PS composite nanofibers shown in Fig. 3d exhibited a two-step weight loss up to 600 °C. The first weight loss began at 300 °C because of carbonization of PAN. The second weight loss began at 360 °C and is attributed to decomposition of the PS phase and carbon that originated from PAN into gaseous CO_2 in the composite nanofibers. The TG analysis indicates that PAN first carbonized, then channels formed by PS decomposition, and finally carbon-free anatase TiO_2 nanofibers formed.[45,46]

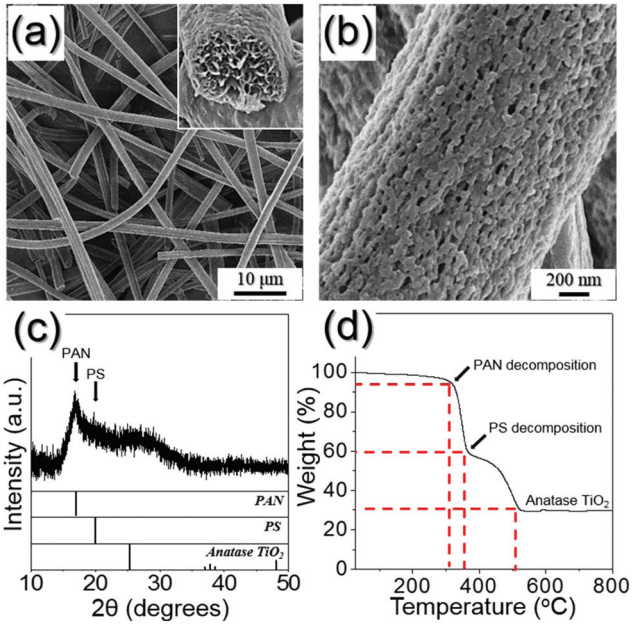

Fig. 3 (a, b) FE-SEM images, (c) XRD pattern, and (d) TG curve of the PAN-TiO_2-PS composite nanofibers obtained after stabilization at 100 °C.

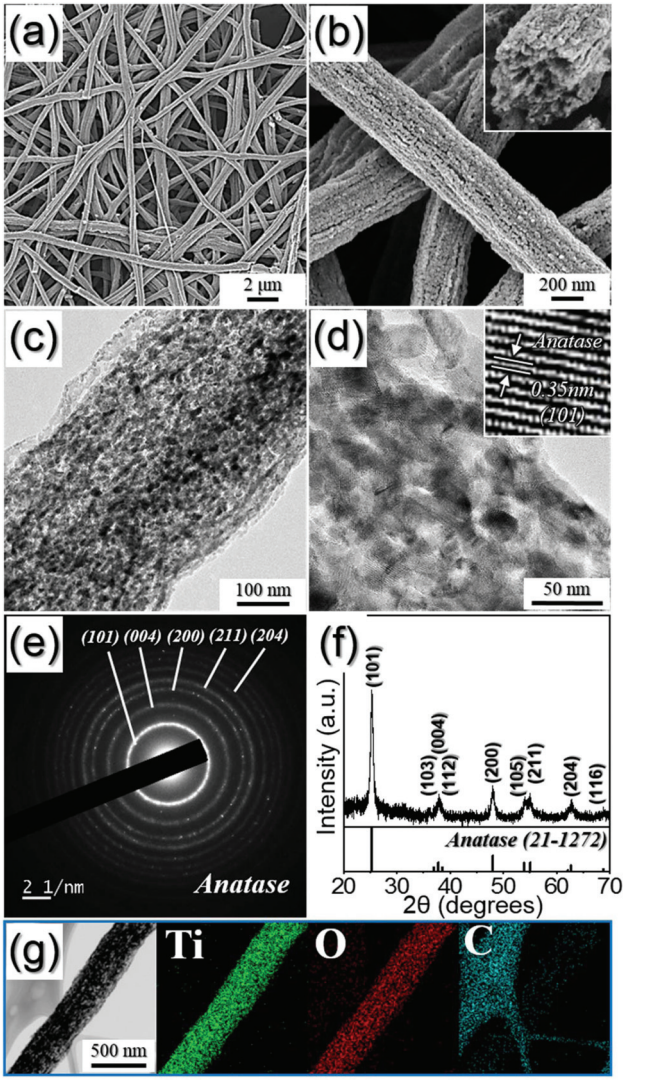

Fig. 4 Morphologies, SAED pattern, and elemental mapping images of IHP-A-TiO_2: (a, b) FE-SEM images, (c, d) HR-TEM images, (e) SAED pattern, (f) XRD pattern, and (g) elemental mapping images.

IHP-A-TiO_2 nanofibers were obtained after heat treating PS-dispersed PAN/TBT composited nanofibers at 500 °C (Fig. 4). The resulting nanofibers had a uniform mean diameter of 380 nm, showed numerous mesopores formed by phase separation of water vapor on the nanofiber surface and interconnected hierarchical pores in the cross-sectional inset images in Fig. 4a and b. Interconnected hierarchical pores (TEM image of Fig. 4c) formed by evaporation of trapped water vapor during stabilization and subsequent PS decomposition during the heat treatment. Numerous mesopores (10–20 nm) were observed in the HR-TEM images shown in Fig. 4c and d. The mean crystallite size of the grains that constituted the nanofibers was 14 nm (Fig. 4d). The HR-TEM inset image shown in Fig. 4d revealed clear lattice fringes separated by 0.35 nm, which correspond to the (101) crystal plane of the tetragonal TiO_2 anatase phase. The selected area diffraction and XRD patterns shown in Fig. 4e and f, respectively, revealed the formation of the pure TiO_2 anatase phase after the heat treatment. The mean crystallite size of the TiO_2 nanocrystals calculated from the half-width of the (101) peak using the Scherrer equation was 13 nm. This agrees with the size determined from the TEM image in Fig. 4d. Complete elimination of the PS and PAN components occurred during the heat treatment to form IHP-A-TiO_2 nanofibers, as shown in the elemental mapping images in Fig. 4g. Ti and O elements were uniformly distributed over the nanostructure, but the C element was negligible in the elemental mapping image. The TG curve of IHP-A-TiO_2 nanofibers also confirmed the complete elimination of PAN and PS during the heat treatment (Fig. S2†).

XPS analysis was performed to confirm the chemical state of IHP-A-TiO_2 nanofibers (Fig. 5). The measured XPS survey spectrum (Fig. 5a) contains signals corresponding to Ti and O elements in the structure.[47] In the Ti 2p spectrum (Fig. 5b), two peaks are located at 463.8 and 458.1 eV, which are attributed to the Ti $2p_{1/2}$ and Ti $2p_{3/2}$ binding energies of anatase TiO_2, respectively.[48,49] Two peaks were also confirmed in the O 1s spectrum (Fig. 5c). The peak at 529.3 eV is attributed to Ti–O binding of the anatase TiO_2 crystal lattice (O–Ti–O). An additional peak was confirmed at 531.0 eV, which is attributed to the hydroxyl group induced by chemically adsorbed H_2O on the anatase sample.[50,51] The N_2 gas adsorption and desorption isotherm and Barrett–Joyner–Halenda pore size distribution of IHP-A-TiO_2 nanofibers are shown in Fig. S3.† The BET surface area of the sample was 43 m^2 g^{-1}, and it contained well-developed mesopores (Fig. S3a†). Therefore, IHP-A-TiO_2 nanofibers containing hierarchical pores originated from the two phase separation process, and sizes between 10 and 120 nm could be

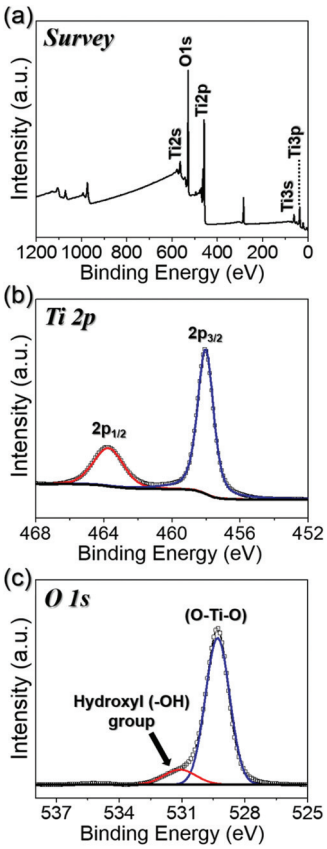

Fig. 5 (a) XPS survey spectrum, (b) XPS Ti 2p spectrum, and (c) XPS O 1s spectrum of IHP-A-TiO_2.

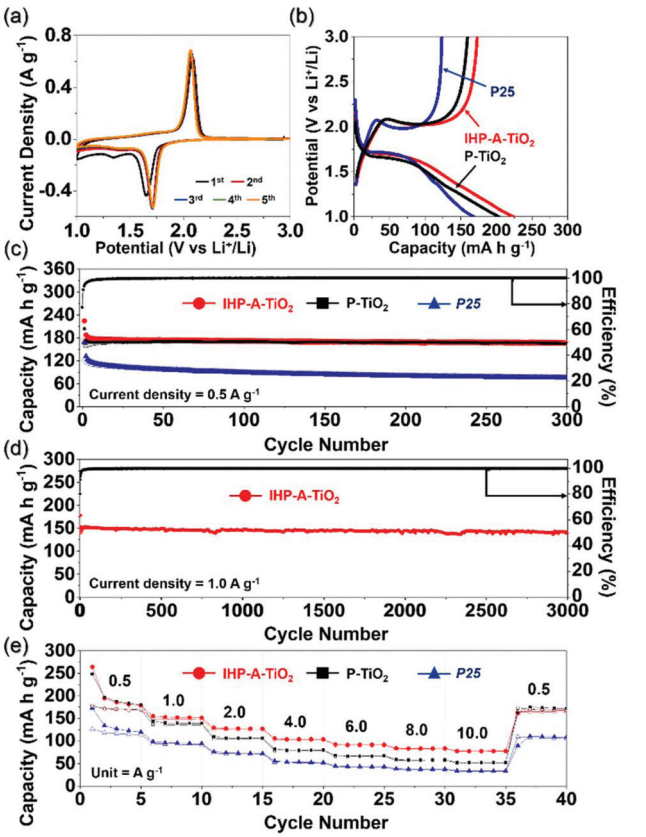

Fig. 6 Electrochemical properties of IHP-A-TiO_2, P-TiO_2, and P25 for lithium ion storage: (a) CV curves of IHP-A-TiO_2, (b) 1st charge/discharge curves at a constant current density of 0.5 A g^{-1}, (c) cycling performances at a constant current density of 0.5 A g^{-1}, (d) cycling performance at a high current density of 1.0 A g^{-1}, and (e) rate performances at different current densities.

confirmed. A commercial TiO_2 nanopowder (P25) was selected to compare its electrochemical properties with those of IHP-A-TiO_2 nanofibers (Fig. S4†). Commercial TiO_2 nanopowders have a mean size of 35 nm and have a mixed crystal structure of anatase and rutile phases (ratio of anatase to rutile is 8 : 2).

The electrochemical properties of IHP-A-TiO_2 nanofibers, P-TiO_2 and commercial TiO_2 nanopowders as comparative samples are shown in Fig. 6. The CV curves of IHP-A-TiO_2 nanofibers were measured from 1.0 to 3.0 V during the first 5 cycles at a scan rate of 0.1 mV s^{-1} (Fig. 6a). The first cathodic scan of IHP-A-TiO_2 nanofibers showed a reduction peak at 1.7 V, and the anodic scan exhibited an oxidation peak at 2.1 V, corresponding to previous studies for anatase TiO_2.[52–54] The reduction peak at 1.7 V was attributed to Li^+ intercalation into the interstitial octahedral site of anatase TiO_2. Unusually, an extra reduction peak was observed at around 1.4 V for the first cathodic scan, which disappeared in the subsequent cycles. It might be attributed to the discrete phase or imperfection in the TiO_2 lattice, which could enable Li^+ ion transport.[55] The initial discharge and charge curves of the two samples at a current density of 0.5 A g^{-1} are shown in Fig. 6b. The obvious discharge plateau at 1.7 V and charge plateau at 2.0 V are characteristic of Li^+ intercalation and deintercalation between tetragonal anatase TiO_2 and orthorhombic $Li_{0.5}TiO_2$.[56,57] IHP-A-TiO_2 nanofibers showed a larger discharge capacity in the initial intercalation step than P25. In the first discharge, the slope below 1.7 V is a typical property of capacitive behavior, which arises from the surface or interfacial storage of Li^+ ions, further indicating the high surface area and smaller TiO_2 crystallite size (13 nm) of IHP-A-TiO_2 nanofibers compared to that of P25 (22 nm).[58,59] In addition, IHP-A-TiO_2 exhibited slightly higher discharge capacity than P-TiO_2 due to the easy penetration of the electrolyte through the interconnected pore structure.[60] P25 powders contain a mixed crystal structure of anatase and rutile phases (ratio of anatase to rutile is 8 : 2). Li^+ ion intercalation is restricted in the rutile phase because of the large difference in the Li^+ ion diffusion coefficients of rutile along the *a* and *c* axis channels.[61,62] Therefore, the rutile phase in the P25 powders interrupted Li^+ ion transport in the intercalation and deintercalation steps and caused the poor electrochemical performance. The initial discharge and charge capacities of IHP-A-TiO_2, P-TiO_2 and P25 were 224, 204 and 168 mA h g^{-1}, respectively, and their corresponding charge capacities were 173, 159 and 123 mA h g^{-1}, respectively. The cycling performances of the three samples at a current density of 0.5 A g^{-1} are shown in Fig. 6c. IHP-A-TiO_2 and P-TiO_2 showed similar cycling performances during 300 cycles in

current density of 0.5 A g^{-1}. The discharge capacity of IHP-A-TiO_2 decreased slightly from 188 to 167 mA h g^{-1} and that of P-TiO_2 also decreased slightly from 174 to 164 mA h g^{-1} from the 2nd cycle to the 300th cycle, whereas that of P25 decreased rapidly from 132 to 76 mA h g^{-1}; their capacity retentions (measured from the second cycle) were 88.8, 94.3 and 57.6%, respectively, in the same cycle range. The capacity fading of P25 was observed because the nano-particulate anode was thoroughly interrupted by agglomeration during cycling, which reduced the electroactive area and deteriorated the irreversible cycle performance.[63,64] However, the superior structural stability and higher interfacial Li^+ ion storage of IHP-A-TiO_2 provided an excellent cycling performance and coulombic efficiencies that approached near 100% after the 20th cycle. The long-term cycling performance and coulombic efficiencies of the IHP-A-TiO_2 at a high current density of 1.0 A g^{-1} are shown in Fig. 6d to demonstrate their superior cycling stability. The discharge capacities of IHP-A-TiO_2 for the 2nd and 3000th cycles were 153 and 142 mA h g^{-1}, respectively, and both showed a capacity retention (measured from the 2nd cycle) of 93%. IHP-A-TiO_2 showed high coulombic efficiencies of more than 99.0% from the 20th cycle at a high current density of 1.0 A g^{-1}. The rate performances of IHP-A-TiO_2, P-TiO_2, and P25 when the current density was increased stepwise from 0.5 to 10.0 A g^{-1} are shown in Fig. 6e. Although IHP-A-TiO_2 and P-TiO_2 exhibited similar cycling performance in Fig. 6c, IHP-A-TiO_2 showed higher capacities compared to P-TiO_2 at higher current densities over 1.0 A g^{-1}. IHP-A-TiO_2 showed final discharge capacities of 178, 151, 127, 104, 91, 83, and 77 mA h g^{-1} at current densities of 0.5, 1.0, 2.0, 4.0, 6.0, 8.0, and 10.0 A g^{-1}, respectively. The discharge capacity of IHP-A-TiO_2 recovered to 168 mA h g^{-1} as the current density returned to 0.5 A g^{-1} after 40 cycles. On the other hand, P-TiO_2 showed final discharge capacities of 180, 139, 106, 80, 67, 58, and 52 mA h g^{-1} at current densities of 0.5, 1.0, 2.0, 4.0, 6.0, 8.0, and 10.0 A g^{-1}, respectively. P25 had a low discharge capacity of 34 mA h g^{-1} at a current density of 10.0 A g^{-1}. The structural merit of IHP-A-TiO_2 with uniformly interconnected mesoporous structures enabled easy penetration of the electrolyte and a shorter diffusion route of Li ion and it resulted in the higher reversible capacities than those of P-TiO_2 and P25, even at high current densities.[60,65] Additionally, IHP-A-TiO_2 showed better electrochemical performances than those of other reported TiO_2 materials with various morphologies (summarized in Table S1†).

EIS measurements were conducted to explain the superior cycling performances of IHP-A-TiO_2. The Nyquist plots shown in Fig. 7 depict compressed semicircles in the medium-frequency range, which describe the charge-transfer resistance (R_{ct}) of the electrode.[66] The Nyquist impedance plots of the two samples were obtained by deconvolution using a Randle-type equivalent-circuit model (Fig. 7a). IHP-A-TiO_2 showed lower charge-transfer resistances than P25 before and after 50 cycles. The R_{ct} values of IHP-A-TiO_2 and P25 after 50 cycles (Fig. 7c) were 46 and 84 Ω, respectively. The smaller R_{ct} values of IHP-A-TiO_2 suggested that the well-interconnected ultrafine TiO_2 nanocrystals within the nanofiber were structurally stabile during cycling and facilitated the facile charge transfer at the electrode–electrolyte interface.[67] The relationships

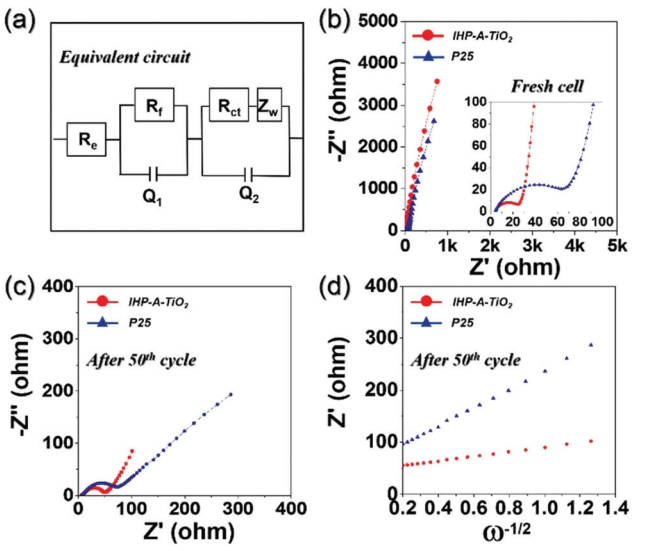

Fig. 7 Nyquist impedance plots and relationships between the real part of the impedance (Z_{re}) and $\omega^{-1/2}$ of IHP-A-TiO_2 and commercial TiO_2 nanopowders (P25); (a) equivalent circuit model used for AC impedance fitting, Nyquist impedance plots (b) before cycling, (c) after 50 cycles, and (d) relationships between the real part of the impedance (Z_{re}) and $\omega^{-1/2}$ after 50th cycles.

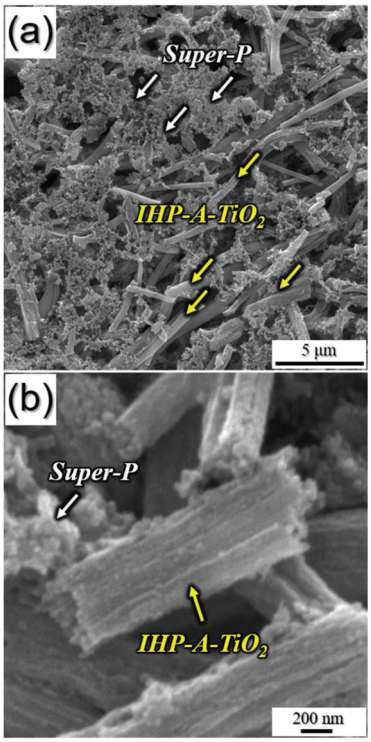

Fig. 8 SEM images of IHP-A-TiO_2 after 100 cycles; (a) low-magnification and (b) high-magnification image.

between the real part of the impedance spectra (Z_{re}) and $\omega^{-1/2}$ (where ω is the angular frequency in the low-frequency region, given by $\omega = 2\pi f$) after 50 cycles are shown in Fig. 7d. IHP-A-TiO_2 showed a faster Li^+ diffusion rate than P25 after cycling. The structural properties of mesoporous nanofibers formed by the synergetic effect of the two kinds of phase separations provided better charge transfer and diffusion performances for IHP-A-TiO_2 than for P25. IHP-A-TiO_2 maintained their morphologies, even after 100 cycles, as shown by the SEM images in Fig. 8. Therefore, IHP-A-TiO_2 that exhibited a low charge transfer resistance and structural stability during cycling had higher capacities and a better cycling stability than commercial TiO_2 nanopowders.

Conclusions

IHP-A-TiO_2 nanofibers prepared by two synergetic effects of phase separation between polymers and RH control during electrospinning were studied as anode materials for LIBs. In this study, PS was added as a dispersed phase in the spinning solution, and it generated channels in the structure during the heat treatment. Additionally, by conducting electrospinning at a high RH of 60%, water vapor-induced phase separation occurred and played an important role in forming numerous mesopores, which interconnected the channels formed by PS decomposition. This new approach is eco-friendly because it requires fewer steps, inexpensive, and does not require chemicals for etching. Well-interconnected ultrafine TiO_2 nanocrystals within the nanofiber provided structural stability during cycling and facilitated the facile charge transfer at the electrode–electrolyte interface as anode materials for LIBs. The method proposed in this study is expected to be very useful for designing and synthesizing nanomaterials that require interconnected and surface-exposed pores in various fields and for various applications, including LIBs.

Conflicts of interest

There are no conflicts to declare.

Acknowledgements

This work was supported by the National Research Foundation of Korea (NRF) grant funded by the Korea government (MSIP) (NRF-2018R1A4A1024691, NRF-2017M1A2A2087577, and NRF-2018R1D1A3B07042514).

Notes and references

1 S. Deville, *Adv. Eng. Mater.*, 2008, **10**, 155–169.
2 E. C. Hammel, O. L.-R. Ighodaro and O. Okoli, *Ceram. Int.*, 2014, **40**, 15351–15370.
3 Y. Lü, W. Zhan, Y. He, Y. Wang, X. Kong, Q. Kuang, Z. Xie and L. Zheng, *ACS Appl. Mater. Interfaces*, 2014, **6**, 4186–4195.
4 S. P. Adiga, L. A. Curtiss, J. W. Elam, M. J. Pellin, C. C. Shih, C. M. Shih, S. J. Lin, Y. Y. Su, S. D. Gittard, J. Zhang and R. J. Narayan, *JOM*, 2008, **60**, 26–32.
5 S. H. Choi, J.-H. Lee and Y. C. Kang, *ACS Nano*, 2015, **9**, 10173–10185.
6 C. M. Parlett, K. Wilson and A. F. Lee, *Chem. Soc. Rev.*, 2013, **42**, 3876–3893.
7 J.-W. Yoon, S. H. Choi, J.-S. Kim, H. W. Jang, Y. C. Kang and J.-H. Lee, *NPG Asia Mater.*, 2016, **8**, e244.
8 B. Zhang, X. Ye, W. Dai, W. Hou and Y. Xie, *Chem. – Eur. J.*, 2006, **12**, 2337–2342.
9 J. S. Cho, J.-S. Park and Y. C. Kang, *Nano Res.*, 2017, **10**, 897–907.
10 Z. Liu, L. Ling, W. Qiao and L. Liu, *Carbon*, 1999, **37**, 663–667.
11 Q. Sun, X.-Q. Zhang, F. Han, W.-C. Li and A.-H. Lu, *J. Mater. Chem.*, 2012, **22**, 17049–17054.
12 H. Tsuchiya and P. Schmuki, *Electrochem. Commun.*, 2005, **7**, 49–52.
13 X. Wang, A. Sumboja, E. Khoo, C. Yan and P. S. Lee, *J. Phys. Chem. C*, 2012, **116**, 4930–4935.
14 L. Zhang, L. Han, S. Liu, C. Zhang and S. Liu, *RSC Adv.*, 2015, **5**, 107313–107317.
15 L. Ji and X. Zhang, *Nanotechnology*, 2009, **20**, 155705.
16 Z. Li, G. Liu, M. Guo, L.-X. Ding, S. Wang and H. Wang, *Electrochim. Acta*, 2015, **173**, 131–138.
17 B. Wang, J. L. Cheng, Y. P. Wu, D. Wang and D. N. He, *Electrochem. Commun.*, 2012, **23**, 5–8.
18 M. Ge, J. Rong, X. Fang and C. Zhou, *Nano Lett.*, 2012, **12**, 2318–2323.
19 L. Ji and X. Zhang, *Electrochem. Commun.*, 2009, **11**, 1146–1149.
20 W. Luo, X. Hu, Y. Sun and Y. Huang, *J. Mater. Chem.*, 2012, **22**, 8916–8921.
21 Y. Tan, Q. Gao, C. Yang, K. Yang, W. Tian and L. Zhu, *Sci. Rep.*, 2015, **5**, 12382.
22 X. Zhang, H. Chen, Y. Xie and J. Guo, *J. Mater. Chem. A*, 2014, **2**, 3912–3918.
23 Y. Liu, X. Yan, B. Xu, J. Lan, Y. Yu, X. Yang, Y. Lin and C. Nan, *ACS Appl. Mater. Interfaces*, 2018, **10**, 19047–19058.
24 Y. Yu, L. Gu, C. Wang, A. Dhanabalan, P. A. Van Aken and J. Maier, *Angew. Chem., Int. Ed.*, 2009, **48**, 6485–6489.
25 L. Ji, Z. Lin, A. J. Medford and X. Zhang, *Carbon*, 2009, **47**, 3346–3354.
26 J. S. Cho, J.-S. Park, K. M. Jeon and Y. C. Kang, *J. Mater. Chem. A*, 2017, **5**, 10632–10639.
27 I. A. Al-Homoudi, J. S. Thakur, R. Naik, G. W. Auner and G. Newaz, *Appl. Surf. Sci.*, 2007, **253**, 8607–8614.
28 I. C. Baek, M. Vithal, J. A. Chang, J.-H. Yum, Md. K. Nazeeruddin, M. Grätzel, Y.-C. Chung and S. I. Seok, *Electrochem. Commun.*, 2009, **11**, 909–912.
29 J. S. Cho, Y. J. Hong and Y. C. Kang, *Chem. – Eur. J.*, 2015, **21**, 11082–11087.

30 S. Kou, W. Ye, X. Guo, X. F. Xu, H. Y. Sun and J. Yang, *RSC Adv.*, 2016, **6**, 39144–39149.
31 X. Xu, G. Yang, J. Liang, S. Ding, C. Tang, H. Yang, W. Yan, G. Yang and D. Yu, *J. Mater. Chem. A*, 2014, **2**, 116–122.
32 Y. Ding, W. Bai, J. Sun, Y. Wu, M. A. Memon, C. Wang, C. Liu, Y. Huang and J. Geng, *ACS Appl. Mater. Interfaces*, 2016, **8**, 12165–12175.
33 H. Kim, M. Y. Cho, M. H. Kim, K. Y. Park, H. Gwon, Y. Lee, K. C. Roh and K. Kang, *Adv. Energy Mater.*, 2013, **3**, 1500–1506.
34 C. Chu, J. Yang, Q. Zhang, N. Wang, F. Niu, X. Xu, J. Yang, W. Fan and Y. Qian, *Appl. Mater. Interfaces*, 2017, **9**, 43648–43656.
35 H.-W. Shim, D. K. Lee, I.-S. Cho, K. S. Hong and D.-W. Kim, *Nanotechnology*, 2010, **21**, 255706.
36 E. Jo, J. G. Yeo, D. K. Kim, J. S. Oh and C. K. Hong, *Polym. Int.*, 2014, **63**, 1471–1477.
37 W. Liu, C. Huang and X. Jin, *Nanoscale Res. Lett.*, 2014, **9**, 350.
38 P. Lu and Y. Xia, *Langmuir*, 2013, **29**, 7070–7078.
39 Y. Cheng, W. Huang, Y. Zhang, L. Zhu, Y. Liu, X. Fan and X. Cao, *CrystEngComm*, 2010, **12**, 2256–2260.
40 Y. Wang, H. Huang, X. Zhao, C. Zou and Y. Xu, *CrystEngComm*, 2016, **18**, 5572–5579.
41 Z. Li, J. T. Zhang, Y. M. Chen, J. Li and X. W. D. Lou, *Nat. Commun.*, 2015, **6**, 8850.
42 S. Li, Y. Dong and M. Guo, *Appl. Surf. Sci.*, 2012, **258**, 8015–8018.
43 X. Lu, H. Mao, W. Zhang and C. Wang, *Mater. Lett.*, 2007, **61**, 2288–2291.
44 D. Zhang, A. B. Karki, D. Rutman, D. P. Young, A. Wang, D. Cocke, T. H. Ho and Z. Guo, *Polymer*, 2009, **50**, 4189–4198.
45 J. S. Cho and Y. C. Kang, *ACS Appl. Mater. Interfaces*, 2016, **8**, 3800–3809.
46 W.-x. Zhang, Y.-z. Wang and C.-f. Sun, *J. Polym. Res.*, 2007, **14**, 467–474.
47 C. W. Lai and S. Sreekantan, *Int. J. Photoenergy*, 2013, **2013**, 276504.
48 K.-H. Choi, N. Duraisamy, N. M. Muhammad, I. Kim, H. Choi and J. Jo, *Appl. Phys. A*, 2012, **107**, 715–722.
49 J. Liu, D. Qian, H. Feng, J. Li, J. Jiang, S. Peng and Y. Liu, *J. Mater. Chem. A*, 2014, **2**, 11372–11381.
50 J. Liang, Y. Feng, G. Liang, Z. Ji, J. Wang, X. Yan and Z. Jin, *J. Mater. Sci. Lett.*, 2003, **22**, 1503–1506.
51 B. Liu, Q. H. L. Wen and X. Zhao, *Thin Solid Films*, 2009, **517**, 6569–6575.
52 Y. B. He, M. Liu, Z. L. Xu, B. Zhang, B. Li, F. Kang and J. K. Kim, *Energy Technol.*, 2013, **1**, 668–674.
53 Z. Wang, X. Li, H. Xu, Y. Yang, Y. Cui, H. Pan, Z. Wang, B. Chen and G. Qian, *J. Mater. Chem. A*, 2014, **2**, 12571–12575.
54 H. Wei, E. F. Rodriguez, A. F. Hollenkamp, A. I. Bhatt, D. Chen and R. A. Caruso, *Adv. Funct. Mater.*, 2017, **27**, 1703270.
55 Z. Wang, J. Sha, E. Liu, C. He, C. Shi, J. Li and N. Zhao, *J. Mater. Chem. A*, 2014, **2**, 8893–8901.
56 W. Li, F. Wang, S. Feng, J. Wang, Z. Sun, B. Li, Y. Li, J. Yang, A. A. Elzatahry, Y. Xia and D. Zhao, *J. Am. Chem. Soc.*, 2013, **135**, 18300–18303.
57 R. Wu, S. Shen, G. Xia, F. Zhu, C. Lastoskie and J. Zhang, *ACS Appl. Mater. Interfaces*, 2016, **8**, 19968–19978.
58 J. Y. Shin, D. Samuelis and J. Maier, *Adv. Funct. Mater.*, 2011, **21**, 3464–3472.
59 D. Wang, D. Choi, J. Li, Z. Yang, Z. Nie, R. Kou, D. Hu, C. Wang, L. V. Saraf, J. Zhang, I. A. Aksay and J. Liu, *ACS Nano*, 2009, **3**, 907–914.
60 X. Xu, F. Niu, D. Zhang, C. Chu, C. Wang, J. Yang and Y. Qian, *J. Power Sources*, 2018, **384**, 240–248.
61 X. Yan, Z. Wang, M. He, Z. Hou, T. Xia, G. Liu and X. Chen, *Energy Technol.*, 2015, **3**, 801–814.
62 H. Yildirim, J. P. Greeley and S. K. R. S. Sankaranarayanan, *Phys. Chem. Chem. Phys.*, 2012, **14**, 4565–4576.
63 Y. Cai, H.-E. Wang, J. Jin, S.-Z. Huang, Y. Yu, Y. Li, S.-P. Feng and B.-L. Su, *Chem. Eng. J.*, 2015, **281**, 844–851.
64 H. Ren, J. Sun, R. Yu, M. Yang, L. Gu, P. Liu, H. Zhao, D. Kisailus and D. Wang, *Chem. Sci.*, 2016, **7**, 793–798.
65 L. Shen, C. Yuan, H. Luo, X. Zhang, K. Xu and Y. Xia, *J. Mater. Chem.*, 2010, **20**, 6998–7004.
66 J. S. Cho, Y. J. Hong and Y. C. Kang, *ACS Nano*, 2015, **9**, 4026–4035.
67 G. D. Park, J. S. Cho and Y. C. Kang, *Nano Energy*, 2015, **17**, 17–26.